Reconstruction of the SNO+ Experiment

Jie Hu

A Dissertation

Presented to the Faculty

of University of Alberta

in Candidacy for the Degree

of Doctor of Philosophy

Recommended for Acceptance

by the Department of

Department of Physics

January, 2019

Abstract

0.1 Abstract

A neutrino is one of the elementary particles we currently know and is included in the Standard Model (SM). However, some properties of neutrinos can not be described by the SM, which shows clues of the new physics beyond the Standard Model.

SNO+ experiment is planned to explore one of the unknown properties of neutrinos: whether the neutrinos are Majorana particles or Dirac particles.

Acknowledgements

Contents

List of Figures

List of Tables

Chapter 1

Introduction

Neutrinos are one of the elementary particles we currently know and are included in the Standard Model (SM). However, some properties of neutrinos can not be described by the SM, which shows clues of the new physics beyond the SM.

SNO+ is a multi-purpose neutrino experiment

SNO+ experiment is planned to explore one of the unknown properties of neutrinos: whether the neutrinos are Majorana particles or Dirac particles.

In this thesis, a position and time reconstruction algorithm is developed for SNO+ physics phases.

calibration

solar neutrino and backgrounds analysis

the SNO+ water phase and partial scintillator fill phase.

1.1   Studies on Solar Neutrinos: History and Current Status

Chapter 2

Neutrino physics

2.1 Neutrino Flavor Transformation and Oscillation

Neutrino oscillation was first discovered in 1998. It is the first direct evidence showing that the Standard Model is incomplete.

The neutrinos generated with definite flavor from weak interactions and related to solar neutrino oscillations

2.1.1 Vacuum Oscillation

2.1.2 Matter Effect

The matter effect is caused by neutrinos interacting with ambient electrons and nucleons in matter such as the Sun or the Earth. ν_e interacts with electrons via both charged weak current (exchanging W boson) and neutral weak current (Z boson) while ν_μ and ν_τ interact only by the neutral current. The ν_e energy has an addition term, $V_{CC} = \sqrt{2}G_F n_e$, where n_e is the number density of the electrons in matter and G_F is the Fermi coupling constant for the weak interaction. This affects the oscillation probabilities for neutrinos propagating in matter compared to vacuum, which is called the Mikheyev-Smirnov-Wolfenstein (MSW) mechanism[37, 36].

In vacuum two-flavor mixing, the Schrödinger equation can be written (in natural

units)[42]:

$$i\frac{d}{dt}\begin{bmatrix} \nu_e \\ \nu_\mu \end{bmatrix} = H_0^f \begin{bmatrix} \nu_e \\ \nu_\mu \end{bmatrix}, \tag{2.1}$$

where

$$
\begin{aligned}
H_0^f &= \frac{1}{2E}\begin{bmatrix} m_1^2\cos^2\theta + m_2^2\sin^2\theta & (m_2^2 - m_1^2)\sin\theta\cos\theta \\ (m_2^2 - m_1^2)\sin\theta\cos\theta & m_1^2\sin 2\theta + m_2^2\cos^2\theta \end{bmatrix} = \\
&\quad \frac{\Delta m_{21}^2}{4E}\begin{bmatrix} -\cos 2\theta & \sin 2\theta \\ \sin 2\theta & \cos 2\theta \end{bmatrix} + \frac{(m_1^2 + m_2^2)}{4E}\begin{bmatrix} 1 & 0 \\ 0 & 1 \end{bmatrix},
\end{aligned}
\tag{2.2}
$$

and $\Delta m_{21}^2 = (m_2^2 - m_1^2)$.

To simplify the calculation, we can drop the second unitary term of H_0^f that is irrelevant to the neutrino flavor transformation. Including the matter effect, we obtain:

$$H_m = \begin{bmatrix} -\frac{\Delta m_{21}^2}{4E}\cos 2\theta + \sqrt{2}G_F n_e & \frac{\Delta m_{21}^2}{4E}\sin 2\theta \\ \frac{\Delta m_{21}^2}{4E}\sin 2\theta & \frac{\Delta m_{21}^2}{4E}\cos 2\theta \end{bmatrix} \tag{2.3}$$

We define a mixing angle in matter, θ_m as:

$$\tan 2\theta_m = \frac{\Delta m^2 \sin 2\theta}{\Delta m^2 \cos 2\theta - 2\sqrt{2}EG_F n_e}, \tag{2.4}$$

and define an effective squared-mass difference in matter Δm_m^2 as:

$$\Delta m_m^2 = \sqrt{(\Delta m^2 \cos 2\theta - 2\sqrt{2}EG_F n_e)^2 + (\Delta m^2 \sin 2\theta)^2}. \tag{2.5}$$

In analogy with mixing in vacuum, we can write the mixing equation relating the energy eigenstates in matter (ν_{1m}, ν_{2m}) to the flavor eigenstates with a diagonalized Hamiltonian:

$$\begin{bmatrix} \nu_e \\ \nu_\mu \end{bmatrix} = \begin{bmatrix} \cos\theta_m & \sin\theta_m \\ -\sin\theta_m & \cos\theta_m \end{bmatrix}\begin{bmatrix} \nu_{1m} \\ \nu_{2m} \end{bmatrix}. \tag{2.6}$$

The probability of flavor transformation in matter is:

$$P_{\nu_e \to \nu_\mu} = \sin^2(2\theta_m)\sin^2\left(\frac{\Delta m_m^2 L}{4E}\right). \tag{2.7}$$

The denominator in equation (2.4) implies a resonance condition:

$$V(n_e) = \sqrt{2}G_F n_e = \frac{\Delta m^2 \cos 2\theta}{2E}.$$ (2.8)

From this condition, for a given E, there is a resonance density n_e^{reson} while for a given n_e, there is a resonance energy E^{reson}. When the resonance condition is satisfied, $\theta_m = \frac{\pi}{4}$ and two flavor neutrinos are maximally mixed, even if the vacuum mixing angle θ is small. This is called matter enhanced neutrino oscillation[37, 18].

2.1.3 Three-flavor Mixing

For three-flavor neutrino mixing, we have[38]:

$$|\nu_f> = \sum_{k=1}^{3} U_{fk}^* |\nu_k>,$$ (2.9)

where $f = e, \mu, \tau$ and $k = 1, 2, 3$. The unitary PMNS matrix, U_{PMNS}, can be parametrized as:

$U_{PMNS} =$

$$\begin{bmatrix} 1 & 0 & 0 \\ 0 & \cos\theta_{23} & \sin\theta_{23} \\ 0 & -\sin\theta_{23} & \cos\theta_{23} \end{bmatrix} \begin{bmatrix} \cos\theta_{13} & 0 & e^{-i\delta_{CP}}\sin\theta_{13} \\ 0 & 1 & 0 \\ e^{-i\delta_{CP}}\sin\theta_{13} & 0 & \cos\theta_{13} \end{bmatrix} \begin{bmatrix} \cos\theta_{12} & \sin\theta_{12} & 0 \\ -\sin\theta_{12} & \cos\theta_{12} & 0 \\ 0 & 0 & 1 \end{bmatrix}.$$ (2.10)

In the PMNS matrix, we have four parameters: the three mixing angles $\theta_{12}, \theta_{13}, \theta_{23}$ and the charge-parity (CP) violation parameter of lepton sector, δ_{CP}. The unknown value of δ_{CP} is related to leptogenesis, the hypothetical physical process that produced an asymmetry between leptons and antileptons in the very early universe[?]. In addition, there are two squared-mass differences, $\Delta m_{21}^2 = m_2^2 - m_1^2$ and $\Delta m_{32}^2 = |m_3^2 - m_2^2|$. The sign of Δm_{32}^2 is unknown and it indicates a mass hierarchy problem of whether neutrino mass is normal hierarchy (NH, $m_3 > m_2 > m_1$) or inverted hierarchy (IH, $m_3 < m_1 < m_2$)[38].

Currently, these six parameters have been measured by neutrino oscillation experiments. These experiments can be classified by the neutrino sources they use. They are the solar, the reactor, the atmospheric, the accelerator and the astronomical neutrino experiments. Table 2.1 lists the energy scale of the neutrino source as well as the example experiments.

Table 2.1:   Oscillation neutrino experiments.

type	source	E_ν	example
solar	the Sun	MeV scale	SNO
reactor	reactor	MeV scale	DayaBay
atmospheric	cosmic-ray	GeV scale	SuperK
accelerator	ν beam from accelerator	GeV scale	T2K
astronomical	astronomical objects	GeV-EeV scale	IceCube

For the Δm_{21}^2 and θ_{12}, the combined analysis of the measurements from the reactor experiment KamLAND and SNO gave $\Delta m_{21}^2 = 7.59_{-0.21}^{+0.21} \times 10^{-5} eV^2$ and $\tan^2 \theta_{21} = 0.47_{-0.05}^{+0.06}$[?].

The accelerator neutrino experiments as well as the atmospheric neutrino experiments have measured Δm_{32}^2 and θ_{23}. The most recent results from SuperK show that in NH, $\sin^2 \theta_{23} = 0.588_{-0.064}^{+0.031}$ and $\Delta m_{32}^2 = 2.5_{-0.20}^{+0.13} \times 10^{-3} eV^2$[?].

In 2012, the reactor neutrino experiment Daya Bay reported the discovery of non-zero θ_{13} with a significance of 5.2σ. In 2016, Daya Bay reported that $\sin^2 2\theta_{13} = 0.0841 \pm 0.0027(stat.) \pm 0.0019(syst.)$. This high-precision result makes $\sin^2 2\theta_{13}$ the best measured mixing angle[?, ?].

δ_{CP} is examined by the experiments which measure the difference between neutrino and antineutrino oscillation probabilities $P(\bar\nu_\alpha \to \bar\nu_\beta)$ and $P(\nu_\alpha \to \nu_\beta)$[?]. In 2017, the T2K experiment in Japan rejected the hypothesis that neutrinos and antineutrinos oscillate with the same probability at 95% confidence (2σ) level. This indicates a hint of CP symmetry broken by neutrinos[?].

The oscillation probability in matter can be written in a concise and exact form as [26]:

$$P(\nu_e \to \nu_\mu) = A \cos \delta + B \sin \delta + C$$

will also provide the information for the CP- and T-violation by investigating the quantities of:

$$A_{CP} = \frac{P(\nu_\alpha \to \nu_\beta) - P(\bar\nu_\alpha \to \bar\nu_\beta)}{P(\nu_\alpha \to \nu_\beta) + P(\bar\nu_\alpha \to \bar\nu_\beta)}$$

$$A_T = \frac{P(\nu_\alpha \to \nu_\beta) - P(\bar{\nu}_\beta \to \bar{\nu}_\alpha)}{P(\nu_\alpha \to \nu_\beta) + P(\bar{\nu}_\beta \to \bar{\nu}_\alpha)}$$

2.1.4   Reactor-solar Experiments

KamLand

Daya Bay

The Jiangmen Underground Neutrino Observatory (JUNO) is a reactor neutrino experiment located at Kaiping, Jiangmen in Southern China. a large liquid scintillator detector large active mass of 20 kton

the energy resolution (3% at 1 MeV) [19]

2.1.5   Atmosphere-accelerator Experiments

2.1.6   Astrophysics Experiments

Neutrino telescopes Ice cube Baikal

2.2   Majorana Neutrino

Dirac equation $(i\gamma^\mu \partial_\mu - m)\psi = 0$, get coupled equations

The interpretation of the $0\nu\beta\beta$ process is considered as exchanging light Majorana neutrinos. In this case the effective Majorana mass $< m_{ee} >= \sum_{i=1}^{3} |U_{ei}|^2 m_i$ $(i = 1, 2, 3)$, where U_{ei} are the elements of the neutrino mixing matrix for the flavor state ν_e, and m_i are the mass eigenvalues of the mass eigenstates (from (2.9)). The observable quantity is the half-life:

$$(T_{1/2}^{0\nu\beta\beta})^{-1} = G_{PS}(Q, Z)|M_{Nuclear}|^2 < m_{ee} >^2,$$

Majorana found a representation of the γ-matrices as follow:

$$\gamma_M^0 = \begin{pmatrix} 0 & \sigma^2 \\ \sigma^2 & 0 \end{pmatrix}, \gamma_M^1 = \begin{pmatrix} \sigma^3 & 0 \\ 0 & \sigma^3 \end{pmatrix}, \gamma_M^2 = \begin{pmatrix} -\sigma^2 & 0 \\ 0 & \sigma^2 \end{pmatrix}, \gamma_M^3 = -i \begin{pmatrix} \sigma^1 & 0 \\ 0 & \sigma^1 \end{pmatrix}$$

These matrices themselves are pure imaginary.

2.3 Double Beta Decay

For heavy radioactive isotopes with nuclei of even neutron number (N) and even proton number (Z) (called even-even nucleus), beta decay will lead to an odd-odd nucleus which is less stable. For some such isotopes the beta decay is energetically forbidden. In 1935, Maria Goeppert-Mayer pointed out that they can still decay through a double beta decay process: $(Z, A) \rightarrow (Z+2, A) + 2e^- + 2\bar{\nu}_e + Q_{\beta\beta}$, where the $Q_{\beta\beta}$ is the released energy. This is called ordinary double beta decay or $2\nu\beta\beta$, which is allowed by the Standard Model and with a typical half-life $T_{1/2} > 10^{19}$ years[**?**].

In 1937, Ettore Majorana proposed that neutral spin-1/2 particles (fermions) can be their own antiparticles[**?**]. If neutrinos have this behaviour, the process called neutrinoless double beta decay ($0\nu\beta\beta$) will also be expected. The Feynman diagrams of $2\nu\beta\beta$ and $0\nu\beta\beta$ are illustrated in Figure **??**.

The interpretation of the $0\nu\beta\beta$ process is considered as exchanging light Majorana neutrinos. In this case the effective Majorana mass $< m_{ee} >= \sum_{i=1}^{3} |U_{ei}|^2 m_i$ $(i = 1, 2, 3)$, U_{ei} are the elements of the neutrino mixing matrix for the flavor state ν_e, and m_i are the mass eigenvalues of the mass eigenstates (from (2.9)). The observable quantity is the half-life:

$$(T_{1/2}^{0\nu\beta\beta})^{-1} = G_{PS}(Q, Z)|M_{Nuclear}|^2 < m_{ee} >^2,$$

where G_{PS} is the phase space factor and $|M_{Nuclear}|$ is the nuclear matrix element for the physics process describing the $0\nu\beta\beta$ decay process[**?**].

Similar to beta decay, the $2\nu\beta\beta$ process will cause a continuous spectrum in the detector while the $0\nu\beta\beta$ process only has two electrons in the final state, which sum up to give a distinct energy peak. By measuring this exact energy, a detector with high energy resolution is able to search for the $0\nu\beta\beta$ signal from the $0\nu\beta\beta$ decay radioactive isotopes. Diverse technologies have been developed during the past decades. The following section lists some

of the mainstream experiments.

$$\Psi_R = \begin{bmatrix} \psi_R \\ \psi_R^C \end{bmatrix}, \Psi_L = \begin{bmatrix} \psi_L \\ \psi_L^C \end{bmatrix}, M = \begin{bmatrix} m_L^M & m^D \\ m^D & m_R^M \end{bmatrix}, \tag{2.11}$$

The mass eigenstates:

$$m_\pm = \frac{1}{2}[\ (m_L^M + m_R^M) \pm \sqrt{(m_L^M - m_R^M)^2 + 4(m^D)^2}\ ],$$

from (2.3), there are 4 cases for discussion:

(1) If $m_L^M = m_R^M = 0$, $m_{1,2} = m^D$, neutrinos are pure Dirac particles.

(2) If $m^D \gg m_{L,R}^M$, $\frac{m^D}{m_{L,R}^M} \to 0$, $m_{1,2} = \frac{1}{2}m^D[\ \frac{(m_L^M + m_R^M)}{m^D} + \sqrt{(\frac{m_L^M - m_R^M}{m^D})^2 + 4}\ ] \approx m^D$, neutrinos are Pseudo-Dirac-Neutrinos.

(3) If $m^D = 0$, $m_1 = m_L^M$, $m_2 = m_R^M$, neutrinos are pure Majorana particles.

(4) In the case of the seesaw mechanism, where $m_R^M \gg m^D, m_L^M = 0$, and for $(\frac{m^D}{m_R^M})^2 \to 0$, use $(1+x)^\alpha \sim 1 + \alpha x$ ($if\ x \to 0$), we get:

$$m_1 = m_- = \frac{\frac{1}{2}[(m_R^M)^2 - (m_R^M)^2 - 4(m^D)^2]}{m_R^M(1 + \sqrt{1 + 4(\frac{m^D}{m_R^M})^2})} \approx -\frac{(m^D)^2}{m_R^M},$$

$$m_2 = m_+ = \frac{1}{2}[m_R^M + m_R^M(1 + \frac{1}{2}(\frac{2m^D}{m_R^M})^2)] = m_R^M[1 + (\frac{m^D}{m_R^M})^2] \approx m_R^M.$$

For $\mathcal{O}(1TeV)$, the ν mass is 0.1 eV

2.3.1   Status of Double Beta Decay Experiments

At the time of writing,

$0\nu\beta\beta$ in the range of $10^{25} - 10^{26}$ year,

The GERmanium Detector Array (GERDA) experiment searches for $0\nu\beta\beta$ of ^{76}Ge. The experiment uses bare germanium crystals with an enrichment of up to $\sim 87\%$ ^{76}Ge operated in a radiopure cryogenic liquid argon (LAr). GERDA Phase I had an exposure of 21.6 kg·yr and Phase-II started with 35.6kg from enriched material in December 2015. With combined data of Phase I and Phase II,

a total exposure of 82.4 kg·yr

GERDA reported in 2019 a lower limit half-life of $T_{1/2}^{0\nu}(^{76}\text{Ge}) > 0.9 \times 10^{26}$ years at 90% C.L.[?, 5].

The Enriched Xenon Observatory (EXO) experiment uses 200-kg liquid Xenon (LXe) time projection chamber (TPC) to search for $0\nu\beta\beta$ in ^{136}Xe. In 2011 they observed the half life of double beta decay of ^{136}Xe to be 2.11×10^{21} years and in 2014 they set a limit on $T_{1/2}^{0\nu}(^{136}\text{Xe}) > 1.1 \times 10^{25}$ yr[?]. EXO is now upgrading to the next 5-tonne experiment (nEXO) and is expected to reach an exclusion sensitivity of $T_{1/2}^{0\nu}(^{136}\text{Xe})$ to about 10^{28} years at 90% C.L.[?].

Also looking into ^{136}Xe, the KamLAND-Zen (ZEroNeutrino) experiment exploits the existing facilities of KamLAND by setting a 3.08-m-diameter spherical inner balloon filled with 13 tons of Xe-loaded liquid scintillator at the center of the KamLAND detector.

liquid scintillator cocktail of 82% decane and 18% pseudocumene by volume, 2.7 g/L PPO.

photocathode coverage of 34%.

Their 2016 results from a 504 kg·yr exposure obtained a lower limit for the $0\nu\beta\beta$ decay half-life of $T_{1/2}^{0\nu}(^{136}\text{Xe}) > 1.07 \times 10^{26}$ yr at 90% C.L. and the corresponding upper limits on the effective Majorana neutrino mass are in the range $61 - 165$ meV[?].

The Particle and Astrophysical Xenon Experiment III (PandaX-III) high pressure gas-phase time projection chamber (TPC)

The Cryogenic Underground Observatory for Rare Events (CUORE) experiment searches for $0\nu\beta\beta$ in ^{130}Te. CUORE is a ton-scale cryogenic bolometer array that arranges 988 tellurium dioxide (TeO_2) crystals. CUORE reported first results in 2017 after a total TeO_2 exposure of 86.3 kg·yr. An effective energy resolution of (7.7 ± 0.5) keV FWHM and a background count of (0.014 ± 0.002) counts/(keVkgyr) in the ROI were achieved in that data exposure. Combined with the early data (the data from the two precursor experiments, Cuoricino and CUORE-0), they placed a lower limit of $T_{1/2}^{0\nu}(^{130}\text{Te}) > 1.5 \times 10^{25}$ yr at 90% C.L. and $m_{\beta\beta} < (110 - 520)$ meV[6]. In five years live time, the experiment will give a projected sensitivity of 9.5×10^{25} yr at the 90% C.L. and set an upper limit on the effective

Majorana mass in the range $50 - 130$ meV[32].

Chapter 3

The SNO+ Experiment

3.1 A Description of SNO+ Detector

3.1.1 Overview

The SNO+ experiment is located at SNOLAB in Vale's Creighton mine in Sudbury, Ontario, Canada. The deep underground facility of the SNOLAB provides a 2092 ± 6 m flat overburden of rock, which is 5890 ± 94 water equivalent meter (w.e.m). This rock overburden ensures an extremely low rate of cosmic muons passing through the detector. The rate is 0.27 $\mu/m^2/day$, compared to an average flux of about 1.44×10^6 $\mu/m^2/day$ at sea level[2].

The detector has been running since December 2016[?],

The SNO+ detector is the successor of the SNO experiment, which makes use of the SNO detector structure.

detector consists of an acrylic vessel (AV) sphere of 12 m in diameter and

5.5 cm in thickness. The AV sphere is concentric within a stainless steel photomultiplier(PMT) support structure (PSUP), which is a geodesic dome with an average radius of 8.4 m. The Hamamatsu 8-inch R1408 PMTs are mounted on the PSUP. 9394 PMTs are looking inward to the AV, giving a 50% effective coverage, while 90 PMTs are looking outward, serving as muon vetos. These two structures are housed in a rock cavity filled

with 7000 tonnes of ultrapure water (UPW) to provide both buoyancy for the vessel and radiation shielding.

main upgrades from SNO to SNO+ BiPo tagging on partial fill data

3.1.2 SNO+ Physics Phases

The SNO+ detector is designed for multi-purpose measurements of neutrino physics. The experiment will go through three phases[?]:

1. Water phase

The AV was filled with about 905 tonnes of ultra pure water (UPW). The detector has been collecting physics data since May 2017.

The main physics goal in this phase is to search for the invisible nucleon decay, which violates baryon number and is a prediction of Grand Unified Theory (GUT). In this decay mode, ^{16}O decays into ^{15}O* or ^{15}O*, which de-excites and produces a γ ray of about 6 MeV.

During the water phase, different types of calibration runs have been taken. The detector responses, systematics and backgrounds are studied. Multiple physics analyses of solar neutrinos, reactor antineutrinos and nucleon decay are going on. The external backgrounds are also measured, which will be the same as the following two phases.

2. Scintillator phase

The AV will be filled with 780 tonnes of liquid scintillator, which is a mixture of linear alkylbenzene (LAB) as a solvent and 2 g/L of 2,5-diphenyloxazole (PPO) as a fluor.

In this phase, the main physics goal is to measure low energy solar neutrinos: the CNO, pep and low energy ^{8}B neutrinos. The pep neutrinos are mono-energetic, with E_ν=1.442 MeV and their flux is well predicted by the Standard Solar Model. A measurement of the pep neutrinos will give more information of the matter effects in neutrino oscillations[?].

The solar metallicity is the abundance of elements heavier than ^{4}He (called "metal" elements in the context of astronomy). It is poorly constrained and the predictions from different solar models disagree with each other. A measurement of the CNO neutrinos can give the abundance of ^{12}C, ^{13}N and ^{15}O and can thus resolve the metallicity problem[?].

Geoneutrino, reactor antineutrino and supernova neutrino detections are additional goals.

A six-month period of scintillator filling and six to twelve months of data-taking are expected for this phase. During the filling, it is planned to operate the partially filled detector at a water level about 4.4 m for about two weeks. This partial filled transition phase is mainly aimed to understand the in-situ backgrounds of scintillator.

3. Tellurium loading phase

In this final phase, 0.5% natural Tellurium by mass will be loaded into the scintillator. Higher loading concentrations would be possible for a further loading plan[31]. The ^{130}Te is a double beta decay isotope. The main purpose in this phase is searching for $0\nu\beta\beta$ in ^{130}Te.

3.1.3 Detection Principle

Optical Cherenkov Radiation Detection

In the SNO+ water phase, the relay on the .

For any charged particle travelling in a transparent medium at an ultrarelativistic speed (a speed greater than the local phase speed of light in the medium), there is an electromagnetic radiation emitted from the medium under the action of the field of the moving particle[28].

$$v > v_p = c/n(\omega)$$

$\cos\theta_c = (1/n\beta)$

where c is the speed of light in vacuum, n is the refraction index of the medium and $v = \beta c$ is the speed of the particle in the medium.

Frank-Tamm formula

For a particle with a charge of ze, the number of photons produced by Cherenkov radiation per unit path lenght and per unit energy interval of the photons is described by :

$$\frac{d^2 N_r}{dE dx} = \frac{\alpha^2 Z^2}{\hbar c} \mu(E)(1 - \frac{1}{\beta^2 n(E)^2})$$

where α is the fine structure constant

For the case of e^- travelling in the water, we can find that 0.262 MeV is the lowest kinetic energy to create Cherenkov radiation, which is called the Cherenkov threshold.

Scintillation Detection

prompt emission of scintillation light, which is called fluorescence delayed emission of scintillation light, which is called delayed fluorescence or phosphorescence.

3.1.4 Electronics

The SNO+ electronics system includes trigger and readout systems, which record the time and charge information of PMT signals. The system can measure signals with a nanosecond-level timing resolution and single-photon level charge resolution and handle a rate of several kHz for normal operations.

burst from supernova

PMTs are Hamamatsu model R1408.

a single RG59/U type 75 Ω coaxial cable

19 crates×16 cards×32 channels = 9728 electronics channels.

Each crate processes 16×32 = 512 PMTs. 9605 channels are actually used and among them, 32 channels are reserved for calibration devices and labelled as FEC Diagnose (FECD) channels

During the experiment running, the maintenance of the electronics is always ongoing.

crate controller card (XL3)

analog master trigger system (MTC/A+) ("+" means an upgrade to SNO MTC/A)

digital master trigger system (MTC/D)

the analog waveforms are summed on the MTC/A+ card, then they are digitized

CAEN v1720 digitizer

TUBii trigger utility board pulsers and delays

DAQ

nearline provides a real-time analysis of the data quality,

trigger system PMT Interface Card (PMTIC) Front End Card (FEC)

NHit20 (N20), NHit100 (N100) trigger pulses.

MTC/A has 3 discriminators: LOW, MED and HI.

Global Trigger (GT) the timing and charge from the fired PMT is digitized and stored.

Nhit means the number of live hit PMTs in the detector for a given event.

dark noise rate is estimated to be 1 kHz.

3.1.5 Optics

Optical parameters

Winston cone

timing

attenuation

scattering

laser pulse diffuser, it can run with different wavelengths: 337, 365, 385, 420, 450 and 500 nm. The laserball

The acrylic of the AV is UV-transparent

3.1.6 Liquid scintillator

Linear Alkyl Benzene (LAB)

is provided by CEPSA Química Bécancour Inc. Organic liquid scintillators The advantages of LAB are:

- It has very low levels of natural radioactive contaminants such as U, Th and K.

- High light yield and attenuation length.

- It has fast timing response different timing spectrum for α and β events, which enables an $\alpha - \beta$ discrimination.

- High flash point and low toxicity for lab safety.

- appropriate density for mechanical stability

- Good stability and chemically compatible with detector materials, mainly the AV.

- Low cost.

Te-loaded liquid scintillator (TeLS)

To load the tellurium into the liquid scintillator, a compound is made by condensation reactions between telluric acid (TeA) and 1,2-butanediol (BD), with N,N-dimethyldodecylamine (DDA) being used as a stabilization agent.

2 g/L PPO gives an absolute light yield of 11900 photons/MeV.

for the partial-fill phase, 0.5 g/L PPO gives Measurements in 0.5 g/L showed a light yield of 52% of 2 g/L, 6190 photons/MeV[24, 40].

Tellurium-loaded 65% of the pure, unloaded scintillator

water-based wavelength shifter

timing profile, the intensity of scintillation light as a function of time

the prompt fluorescence intensity at a time t excitation be $I = I_0 e^{-\frac{t}{\tau}}$

singlet and triplet states ionization density depend α-particle high ionization density quenching,

3.1.7 Calibration

Two kinds of calibration sources are used by SNO+: optical sources and radioactive sources. The optical sources are used to calibrate the PMT response and to measure the optical properties of the

The radioactive sources are used to calibrate the energy

reconstruction performances and uncertainties. particle identifications
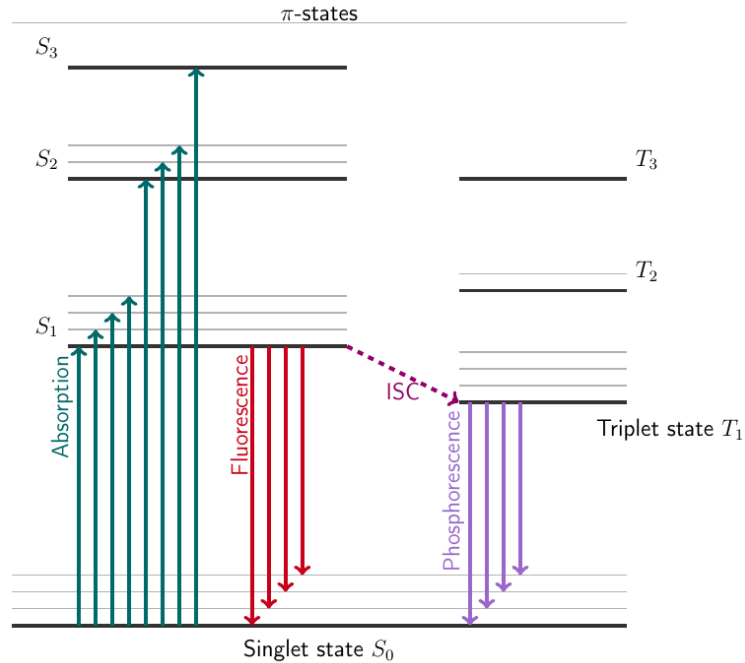
Figure 3.1: A Jablonski diagram for the liquid scintillator, modified from [11, 27].

Calibration sources with known physics parameters: help to understand the detector response to the events and to make accurate measurements Two types of SNO+ calibration sources: optical sources and radioactive sources Optical sources: phototube response, optical properties of the detector media Radioactive source: energy scale, resolution, systematic uncertainties 16N calibration source is one of the radioactive sources

[17]

Optical calibration *in-situ*

- Timing module for the Embedded LED Light Injection Entity (TELLIE)

  light-emitting diode (LED)

  time calibration, time response

  a precision of $\mathcal{O}(1\ ns)$

  Blinky fibre optics nailed to the PSUP to calibrate stuff.

-

•

Calibration source

The ^{16}N source ^{3}H$(p, \gamma)^4$He reaction.

the SNO+ Source Manipulator System (SMS) is inherited from the SNO.

A Umbilical Retrieval Mechanism (URM) is used to send the source down to the inner vessel.

The sources are connected to the umbilical.

An umbilical encloses electrical cables, optical fibres and gas lines connected to the source.

A Universal Interface (UI) connecting the URM and the detector, Therefore, sealed environment, which ensures radon gas not leaking into the detector when deploying the source.

-

3.2   Monte Carlo Simulation for SNO+

The SNO+ collaboration has developed a software framework, called the Reactor Analysis Tool (RAT), which integrates a Monte Carlo simulation of the SNO+ detector and event-based analysis tools (for online and offline event analysis) since the beginning of the program. This software was originally developed by Stan Seibert for Braidwood Collaboration for a generic KamLAND like detector. It is also used by the other astroparticle physics experiemnts, such as DEAP/CLEAN, CLEAR and potentially for Darkside-50.

Geant4 Toolkit and incorporates ROOT libraries for data handling and analysis.

The RAT Monte Carlo was originally developed for the Braidwood Collaboration utilising software developed for a generic KamLAND like detector, called Generic Liquid Scintillator GEANT4 simulation (GLG4). It was branched and developed into the specialist SNO+ version, starting in 2006/2007.

GLG4sim

Braidwood

combines both Monte Carlo simulation of the Braidwood detector with event-based analysis tasks, like reconstruction. The primary goals are:

Make it easy to analyze Monte Carlo-generated events as well as data from disk using the same software with only a few command changes. Even in the proposal R&D phase, where there is no real data, this is still useful for dumping Monte Carlo events to disk to be analyzed by another job. When there is real data, being able to do the analysis with the same code path as was used on Monte Carlo is very reassuring. Allow for a modular, user-controlled analysis of events. This includes allowing the user to selected which analysis tasks to perform (different fitters, pruning unneeded data from the event data structure, etc.). It should also be relatively straightforward for users to introduce their own code into the analysis process. Separate analysis into small tasks which can be developed asynchronously by different people, yet integrated with minimal (or perhaps zero) pain. Integrate into existing GEANT4 and GLG4sim efforts with a minimum of code duplication. As much as possible, RAT should be designed incorporate upgrades of these packages just by relinking. No cut and paste of code (mainly a question with GLG4sim). Design[3]

Chapter 4

Event Reconstruction

4.1 Reconstruction of the SNO+

event vertex

4.2 Reconstruction Algorithms for Position, Time and Energy of Events in SNO+

4.3 Multi-path Vertex Reconstruction Algorithm for SNO+

A Multi-path (MP) reconstruction framework was developed by the University of Alberta group as an additional vertex reconstruction algorithm for SNO+. This framework was first developed by Aksel Hallin to reconstruct and investigate the event vertex for the data taken from an early stage of SNO+ when the detector was partially filled with water at the end of 2014[21]. It was further developed by David Auty and Kalpana Singh for investigating the wavelength shifter and water events[9, 34, 35, 1]. Jeff Tseng restructured the related codes into more flexible and efficient C++ codes and implemented into the RAT software[23].

In this framework, the fitter is adapted for various SNO+ physics phases, including the water phase, a conceptual wavelength shifter (WLS) phase, the partial-fill phase and the scintillator phase (with and without Tellurium loaded). In the SNO+ water phase, the

cavity and the AV are both filled with ultra-pure water. This is a relatively simple geometry since everything inside the PSUP can be simplified as water. Therefore, we start with the MP water fitter (the MPW fitter) to explain the reconstruction concepts.

The MPW fitter fits for position, time and direction of an event in SNO+ water phase. First, the fitter throws a random position built up by random variables which are uniformly distributed inside a sphere with a radius of 10 $meters$ (larger than the actual PSUP radius $r_{PSUP} = 8.39\ m$). Meanwhile, a random event time is also generated, following a uniform distribution in a range of 100 to 300 ns. The Class Library for High Energy Physics (CLHEP) is used for creating pseudo-random numbers (see the Appendix A.1 for details). With random event position and time, a random vertex works as a trial event vertex.

Connecting the trial event vertex to the triggered PMTs, the fitter evaluates a timing parameter, called the time residual (t_{res}), by calculating the time of flight for photons travelling along the paths between the event position to the triggered PMT positions (light paths).

The time residual is defined as:

$$t_{res} = t_{PMT} - t_{transit} - t_{event},$$

where t_{PMT} is the PMT triggered time recorded by the detector, t_{event} is the time when an event occurs, and $t_{transit}$ is the total transit time (or time of flight) taken by a photon travelling from the event position ($\vec{x}_{event}$) to the triggered PMT ($\vec{x}_{PMT}$) and crossing different materials in the detector.

To calculate the $t_{transit}$, the fitter uses photons from prompt time window (prompt light) and assumes that photons propagate in straight lines (straight light paths). Here it is simple: $t_{transit} = |\vec{x}_{event} - \vec{x}_{PMT}|/v_{water}$. Detailed calculations, such as the refraction and reflection when the lights cross different detector materials, absorptions and scatterings from the materials, as well as the lensing effects caused by the spherical structure of the acrylic vessel, are neglected. We found that without these details, the fitter can still produce results consistent with the ones using detailed calculations. For a trial vertex $(\vec{x}_0, t_0)$, the fitter calculates a set of t_{res} values with respect to all the triggered PMTs. These values

are fed into a likelihood function:

$$\ln \mathcal{L}(\vec{x}_0, t_0) = \sum_{i=1}^{\text{Nhits}} \ln P(t_{res}^i),$$

where t_{res}^i is the time residual calculated from the ith triggered PMT and Nhits here stands for the number of total triggered PMTs by an event.

A pre-set 1 dimension (1D) probability density function (PDF) comes from the timing profile measurement and the measured detector response.

$P(t_{res}^i)$ is the probability returned from the PDF for the ith triggered PMT and a trial event vertex.

The Levenberg-Marquardt method, which is commonly used for fitting the nonlinear model for multiple parameters, is used here as an optimizer

used to find the event position and time which maximises the log likelihood when comparing the time residuals to the scintillation time PDF:

As we will see in the following sections, one of the biggest jobs for the fitter is to calculate the $t_{transit}$ by evaluating light paths. In the water phase, we consider photons created in an event travelling along straight line paths and the paths are always in water. In the other situations, for example, when the acrylic vessel is filled with the wavelength shifter or scintillator, the light path calculations will be modified.

Then it utilizes the to maximize the likelihood functions and find the best-fit values.

Figure. **??** shows the reconstruction concepts for position and direction.

Fitter Structure   The MPW fitter consists of:

- Fitter Data : Includes physics constants, set-values and pdfs for the MPW fitter. These parameters are set in the MPW database.

  - Water reflection index (water_RI, or n_{water}), used for group velocity ($v_g =$c$/$n$_{water}$) calculation.

  The MPW fitter currently uses one fixed number for n$_{water}$, rather than a function of wavelengths. The value of n$_{water}$ can be tuned to give the lowest biases of the

fitted positions to the Monte Carlo and to give the lowest RMS of fitted results as well. But the effect of n_{water} can also be corrected by the drive correction afterwards. Currently $n_{water} = 1.38486$ is obtained by analyzing the time of flight from the ^{16}N central run-100934 data reconstructed by the MPW fitter.

- Constants for fit setting: Includes the fitter tolerance, the maximum iterations for the Multi-path Fitter to converge, time offset, radius cut for position vertex, fitting bin-width and steps.

- Other physics constants: air reflection index (air_RI), psup radius.

- PMT response time (timing) pdf for the position reconstruction, as shown in 4.1. The pdf shown in red line is modified from the measured PMT response time distribution from SNO time and the late light response is forced to be de-weighted (black). The pdf is modified in [-100,-4] ns region to match the time residual spectrum obtained from

Figure 4.1: PMT response time as the timing pdf.

- PMT angular response pdf for the direction reconstruction, as shown in 4.2. It is taken from the Monte Carlo simulation of 5 MeV electrons traverse in the AV with one direction.

Figure 4.2: PMT angular distribution as the angular response pdf.

• Fit the position, time and direction.

- Likelihood Calculation Classes: Constructs likelihood functions, calculates likelihoods and their derivatives. For the MPW fitter, there are two classes: WaterPosition for position reconstruction and WaterDirection for direction reconstruction. The WaterPosition class tackles with 4 parameters (x,y,z,t) and the WaterDirection class tackles with 2 parameters (θ, ϕ).

- Multi-path Fitter: Processes the MPW fitter and finds the best-fit of the likelihood function. It is a general processor and is shared with the fitters using the Multi-path

Fitter, including the MPW fitter, air-water (AW) fitter, wavelength-shifter (WLS) fitter and scint-water fitter (being developed). It processes a certain fitter by being assigned the fitter name in macro. It processes the fitter event by event: for every triggered event, it first calls PMT selectors (ModeCut or StraightTimeResidualCut) and sends the information of the reduced PMTs to a certain Likelihood Calculation Class for likelihood calculations. The Likelihood Calculation Class sends back the values of likelihoods and their derivatives, so the Multi-path Fitter does not care about how the likelihood functions are constructed and how the likelihoods and derivatives are calculated. Using these values, it constructs an n×n Hessian matrix (n is the number of fitting parameters defined in Likelihood Calculation Class) and uses the Levenberg-Marquardt (MRQ) method to maximize the likelihood and finds the best-fit values. For the MPW, if the likelihood maxima is found 5 times for any position and direction then values are returned as the fitted position and direction. For the MPW case, it calls the ModeCut and fitsfor the position and time; then it calls the StraightTimeResidualCut and fits for the directions.

- Dump Likelihood: It is a function inside the Multi-path Fitter. It stores the likelihood surfaces and their derivatives from the fitting of the Multi-path Fitter to check whether the fitter finds global or local maximum of the interested events and to check the reconstruction performances. It requires a switch on/off parameter and the GTIDs of the interested events (a list of GTIDs) from the MPW database.

- SDecompQRH: It is a fit method class modified from ROOT TDecompQRH. It is used by the Multi-path Fitter to invert the Hessian matrix. Compared to ROOT, Solve() for Ax=b is modified to zero the component of x for which the diagonal element in R is small. This allows a Levenberg-Marquardt optimization to continue in many cases when the matrix is singular. For the MPW case, it is used to invert 4×4 matrix of the WaterPosition Class while the inversion of 2×2 matrix of the WaterDirection is calculated directly.

- ModeCut: The same class used by Rat. Selects the PMTs of an event by a mode

time window. For the MPW, the optimized window is $[-50 + t_{mode}, 100 + t_{mode}]$ ns obtained from

- StraightTimeResidualCut: Selects the PMTs of an event by a time residue window. This selector requires a fitted position and fitted time. It calculates the time residue directly by assuming straight light path, which is the same method used by Multi-path fitter. For the MPW case, it is used for the direction fit after the position and time are reconstructed. The default window is [-10, 250] ns.

MPW: Position and Direction Reconstructions For the position reconstruction of the MPW fitter, the likelihood function simply calculates the likelihood assuming straight line paths of prompt light from a position vertex $\vec{X}_0$ (fVertex) and a starting time offset t_0 to each of the hit PMTs.

We define the position difference $\vec{X}_{\mathrm{diffCh}} = \vec{X}_0 - \vec{X}_{\mathrm{pmt}}$, then the time of flight for prompt light is $t_{\mathrm{Ch}} = |\vec{X}_{\mathrm{diffCh}}|/v_g$ and $L_{\mathrm{Ch}} = L(t_{\mathrm{Ch}})$.

The derivatives of the likelihood function can be calculated from explicit mathematical forms as:

$$\frac{\partial L}{\partial t_0} = \frac{dL_{\mathrm{Ch}}}{dt_{\mathrm{Ch}}},$$

$$\frac{\partial L}{\partial x} = \frac{\partial L_{\mathrm{Ch}}}{\partial t_{\mathrm{Ch}}}\frac{dt_{\mathrm{Ch}}}{\partial x} = -\frac{dL_{\mathrm{Ch}}}{dt_{\mathrm{Ch}}}\frac{X_{\mathrm{diffCh}}}{|\vec{X}_{\mathrm{diffCh}}| \cdot v_g},$$

$$\frac{\partial L}{\partial y} = -\frac{dL_{\mathrm{Ch}}}{dt_{\mathrm{Ch}}}\frac{Y_{\mathrm{diffCh}}}{|\vec{X}_{\mathrm{diffCh}}| \cdot v_g},$$

$$\frac{\partial L}{\partial z} = -\frac{dL_{\mathrm{Ch}}}{dt_{\mathrm{Ch}}}\frac{Z_{\mathrm{diffCh}}}{|\vec{X}_{\mathrm{diffCh}}| \cdot v_g},$$

where $\frac{dL_{\mathrm{Ch}}}{dt_{\mathrm{Ch}}}$ can be calculated numerically from the timing pdf.

In the WaterPosition class, it starts with a random $(\vec{x}_0, t_0)$ as seed and calculates the likelihoods and their derivatives for various paths. These values are sent to the Multi-path Fitter, which is fitting 4 parameters: x, y, z, t and to maximize the likelihood function through the MRQ method and to find the best-fit positions.

For the direction reconstruction, the direction vertex $\vec{u}_0 = (\cos\phi\sin\theta, \sin\phi\sin\theta, \cos\theta)$ (fDirection), where the θ is zenith angle and ϕ the azimuth. $\cos\theta_{\mathrm{Ch}}$ is the angle between $\vec{u}_0$ and $\vec{X}_{\mathrm{diffCh}}$, which is taken as the fitting parameter of the likelihood function for the direction reconstruction. For the i-th hit PMT, $\cos\theta_{\mathrm{Ch}}^i = \vec{u}_0 \cdot \frac{\vec{X}_{\mathrm{diffCh}}^i}{|\vec{X}_{\mathrm{diffCh}}^i|}$, then the likelihood function is:

$$L(\vec{u}_0) = \sum_{i=1}^{\mathrm{Nhits}} L_i(\cos\theta_{\mathrm{Ch}}^i),$$

The derivatives have explicit mathematical forms:

$$\frac{\partial L}{\partial\theta} = \frac{dL_{\mathrm{Ch}}}{d\cos\theta_{\mathrm{Ch}}}\frac{d\cos\theta_{\mathrm{Ch}}}{\partial\theta} = \frac{dL_{\mathrm{Ch}}}{d\cos\theta_{\mathrm{Ch}}}\frac{d\vec{u}_0}{d\theta}\cdot\frac{\vec{X}_{\mathrm{diffCh}}}{|\vec{X}_{\mathrm{diffCh}}|},$$

where $d\vec{u}_0/d\theta = (\cos\phi\cos\theta, \sin\phi\cos\theta, -\sin\theta)$ and

$$\frac{\partial L}{\partial\phi} = \frac{dL_{\mathrm{Ch}}}{d\cos\theta_{\mathrm{Ch}}}\frac{d\cos\theta_{\mathrm{Ch}}}{d\phi} = \frac{dL_{\mathrm{Ch}}}{d\cos\theta_{\mathrm{Ch}}}\frac{d\vec{u}_0}{d\phi}\cdot\frac{\vec{X}_{\mathrm{diffCh}}}{|\vec{X}_{\mathrm{diffCh}}|},$$

where $d\vec{u}_0/d\phi = (-\sin\phi\sin\theta, \cos\phi\sin\theta, 0)$. $\frac{dL_{\mathrm{Ch}}}{d\cos\theta_{\mathrm{Ch}}}$ can be calculated numerically from the PMT angular response pdf.

In the FitterWaterDirection class, it starts with a random (θ_0, ϕ_0) as seed and calculates the likelihoods and their derivatives for various paths. These values are sent to the Multi-path Fitter, which is now fitting 2 parameters: (θ, ϕ) and to maximize the likelihood function through the MRQ method and to find the best-fit directions.

Drive Correction Once the MPW fitter obtains the fitted position and direction, a drive correction is applied on the fitted position by $\vec{X}_{\mathrm{corrected}} = p_0\vec{X}_{fit} + p_1\vec{u}_{fit}$, where p_0 and p_1 are the correction parameters.

To obtain the values of p_0 and p_1, we generated electron events distributed isotropically inside the AV. The simulations of 2, 3, 4, ... ,10 MeV electrons are produced. Then the MPW fitter is applied on each simulations and returns the results of $\vec{X}_{fit}$ and $\vec{u}_{fit}$. Take the Monte Carlo generated positions $\vec{X}_{MC}$ as the true positions, for all the fitted events, a χ^2 function is calculated by:

$$\chi^2 = \sum_{i=1}^{N_{\mathrm{events}}} [\vec{X}_{MC}^i - (p_0\vec{X}_{fit}^i + p_1\vec{u}_{fit}^i)]^2$$

The p_0 and p_1 are obtained by minimizing the χ^2 function. When doing the χ^2 calculation, the fitted events of $|\vec{X}_{fit} - \vec{X}_{MC}| > 3\ m$ are thrown away to improve the χ^2 minimization results.

For the 2 to 10 MeV electrons simulations, the obtained values of p_0 and p_1 are energy or Nhit dependent. However, it does not improve the results if using the Nhit dependent functions $p_0(Nhit)$ and $p_1(Nhit)$ as drive corrections. Finally we take the average values from the 5 to 10 MeV electrons simulations and the drive correction is set as $\vec{X}_{\text{corrected}} = 0.995765\vec{X}_{fit} + -63.826\vec{u}_{fit}$.

It is important to note that since the drive correction parameters are obtained from the reconstructions of Monte Carlo, it depends on the Monte Carlo and the results of reconstruction. Therefore, the n_{water}, mode cut and time residue cut affecting the fitted results will also affect the drive correction parameters, but not significantly.

By fitting the simulations of 5 MeV electrons generated at the detector center and travelling along +X direction, the drive effct of the MPW fitter causes a $\sim$50 mm biases from the detector center along +X axis. The drive correction reduces this drive bias down to $\sim$0.2 mm. For the reconstruction of ^{16}N data, the drive correction can reduce the fitted position RMS by $\sim$20 mm.

4.4 ^{16}N test

The ^{16}N calibration runs provide an ideal test of fitter performance. From a comparison of reconstructions for data and MC, we can also extract the resolution and bias of the fitter.

The γ rays emitted from the ^{16}N source interact with the water in the detector mainly via Compton scattering. Figure **??** shows the spatial distributions of the first γ-ray interaction positions projected on the x axis (called spatial distribution $S(x)$) obtained from MC simulation. The ^{16}N source is considered as an electron source with a known spatial distribution[**?**]. For simplicity, in the following we always discuss the x component of the position vector $\vec{X}$.

A position resolution function is defined for the reconstructed electron position distribution[?]:

$$R(x) = \frac{1 - \alpha_e}{\sqrt{2\pi}\sigma_p} \exp\left[-\frac{1}{2}(\frac{x - \mu_p}{\sigma_p})^2\right] + \frac{\alpha_e}{2\tau_p} \exp\left[\frac{-|x - \mu_p|}{\tau_p}\right],$$

where α_e is the fractional exponential component, σ_p is the Gaussian width (corresponding to the position resolution), μ_p is the Gaussian shift (corresponding to the position bias) and τ_p is the exponential slope (corresponding to the position distributions in tails).

For electrons from the ^{16}N calibration source, their spatial distribution function $N_R(x)$ can be described by the position resolution function smeared by the convolution of $S(x)$ as[?]:

$$N_R(x) = \int_{-\infty}^{+\infty} S(x)R(x_{fit} - x)dx.$$

Since the $S(x)$ and $N_R(x)$ are histograms obtained from the data and MC, we calculate by the bin value x_i:

$$N_R(x_i) = \sum_{x_i=-\infty}^{+\infty} S(x_i)R(x_{fit}^i - x_i).$$

.

The χ^2 is calculated by:

$$\chi^2 = \sum_{i=0}^{N_{bins}} \left[\frac{N_R(x_{fit}^i) - N_R^{fit}(x_{fit}^i)}{\sigma_i}\right]^2,$$

where N_R^{fit} is a trial fit to the N_R by tuning the $\{\alpha_e, \mu_p, \sigma_p, \tau_p\}$ and σ_i is taken as the bin width of the histograms.

By minimizing the χ^2, the parameters of the resolution function, $\{\alpha_e, \mu_p, \sigma_p, \tau_p\}$ and a best N_R^{fit} are obtained.

Figure ?? shows a comparison of the reconstructed x position of ^{16}N events between data and MC. The reconstructed position distributions are fitted with N_R^{fit}.

Table 4.1 summarizes the values of position resolution parameters obtained from data and MC of ^{16}N calibration runs at the detector center.

Vertex likelihood surface for an typical ^{16}N event (calibration run-100934_s000_p001, event GTID = 61836), projected on X-Y, X-Z and Y-Z planes. A clean global maxima

Table 4.1: Position resolution parameters for the MP Water Fitter.

MPW fitter	α_e	σ_P (mm)	τ_P (mm)	μ_P (mm)
data	0.58±0.04	175.8±3.8	288.0±5.7	-28.8±1.0
MC	0.51±0.05	195.2±3.3	298.4±6.1	-10.9±1.0

gives the reconstructed vertex: the fitted position is at (-211.958, 503.399, 275.990) mm and the fitted time at 217.03885 ns. This is shown in Fig. 4.3.

4.5   Vertex Reconstruction for the SNO+ Partial-phase

For the partial-phase geometry, the SNO+ acrylic vessel can be considered as composed of the neck (cylinder), AV sphere and water-scintillator interface (plane). The ray coming from the vertex to the PMT can intersect with these three geometries.

line-sphere intersection and line-plane intersection

a_1, a_2 and a_3

trial position $\vec{X}_0 = (x_0, y_0, z_0)$, PMT position $\vec{X}_{\mathrm{pmt}} = (x_{\mathrm{pmt}}, y_{\mathrm{pmt}}, z_{\mathrm{pmt}})$

ray-vector $\vec{l}_0 = \vec{X}_0 + a \cdot \vec{u}$, where a is the distance between vertex and intersection point. It is the parameter to be determined. $\vec{u} = (\vec{X}_{\mathrm{pmt}} - \vec{X}_0)$ is the direction of the ray-vector/light path.

$\vec{O}_{av}$ is the origin of the AV sphere. In the PSUP coordinate, $\vec{O}_{av} = (0, 0, 108)$ mm. For the ray-sphere intersection, $(\vec{l}_0 - \vec{O}_{av})^2 = r_{av}^2$

To solve this equation, let $\Delta = \left[(\vec{X}_0 - \vec{O}_{av}) \cdot \vec{u}\right]^2 - \left(\vec{X}_0 - \vec{O}_{av}\right)^2 + r_{av}^2$ then

$$a_{+,-} = -(\vec{X}_0 - \vec{O}_{av}) \cdot \vec{u} \pm \sqrt{\Delta}, \ if \Delta > 0$$

if $\Delta \leq 0$, there is no intersection point or only one intersection point at the AV, the ray never passes through the AV sphere.

For the ray-plane intersection, $l_{0,z} = Z_{split}$, where Z_{split} is the water level. If $u_z = z_{\mathrm{pmt}} - z_0 = 0$, the ray is parallel to the plane and never intersects the plane. To solve this equation, we have $a = (Z_{split} - z_0)/u_z = (Z_{split} - z_0)$, $\ if \ u_z \neq 0$. Let:

$$a_3 \equiv a = \frac{(Z_{split} - z_0)|\vec{X}_{\mathrm{pmt}} - \vec{X}_0|}{z_{\mathrm{pmt}} - z_0} \ \ (if \ z_{\mathrm{pmt}} - z_0 \neq 0),$$
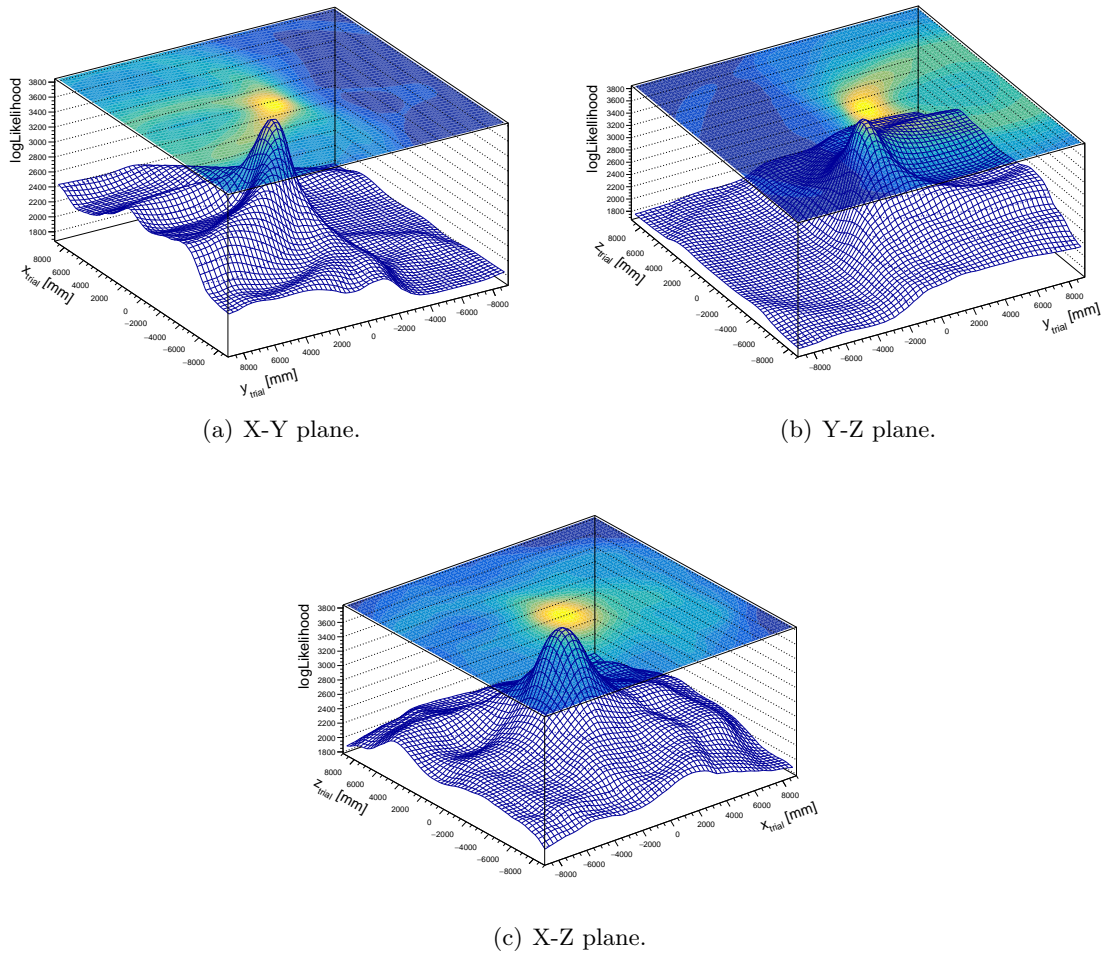
(a) X-Y plane.

(b) Y-Z plane.

(c) X-Z plane.

Figure 4.3: Likelihood surface of an ^{16}N event projected on X-Y, Y-Z, X-Z planes. A clear global maxima is reached for the fitted vertex.
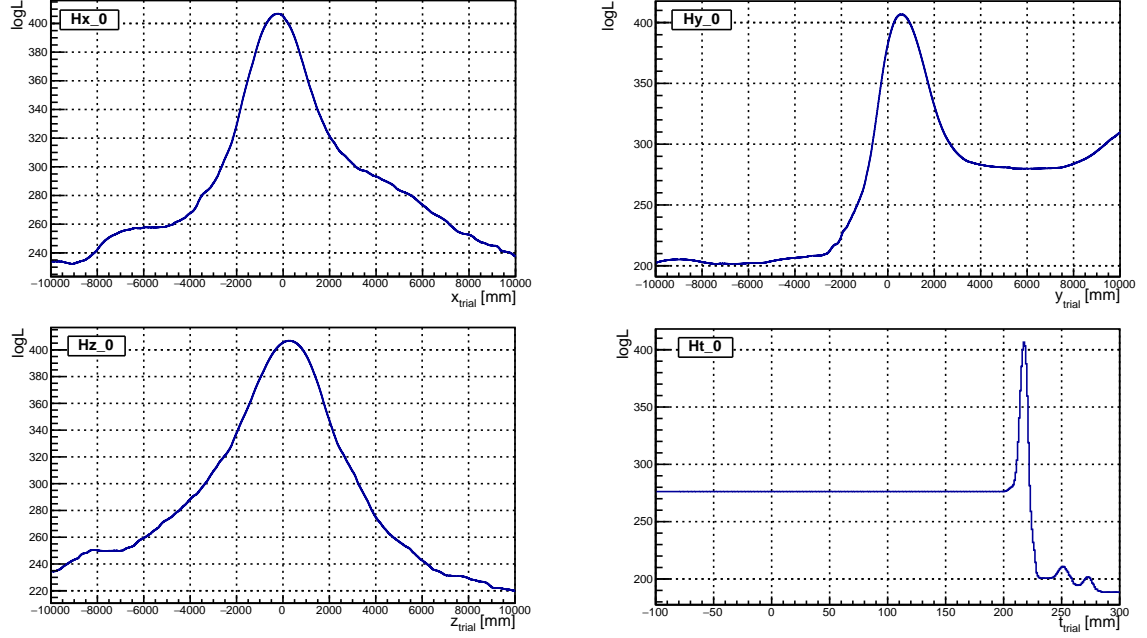
Figure 4.4: Likelihood surface of an ^{16}N event projected on x, y, z, t axes.

For the ray-cylinder intersection, $l_{0,x}^2 + l_{0,y}^2 = r_{neck}^2$, where r_{neck} is the radius of the neck cylinder.

$$time\ of\ flight\ (tof) = (a_+ - a_3)/v_{gr,scint} + [|\vec{X}_{\mathrm{pmt}} - \vec{X}_0| - (a_+ - a_3)]/v_{gr,water}$$

$$\frac{\partial L}{\partial splitZ} = \frac{\partial L}{\partial tof} \cdot \frac{\partial tof}{\partial splitZ} = \frac{\partial L}{\partial tof} \cdot \frac{\partial a_3}{\partial splitZ}$$

$$\frac{\partial L}{\partial splitZ} = 0$$

the optical response of the liquid scintillator

empirical model. This model consists n ($n = 3\ or\ 4$) exponential decays with a common rise time [10].
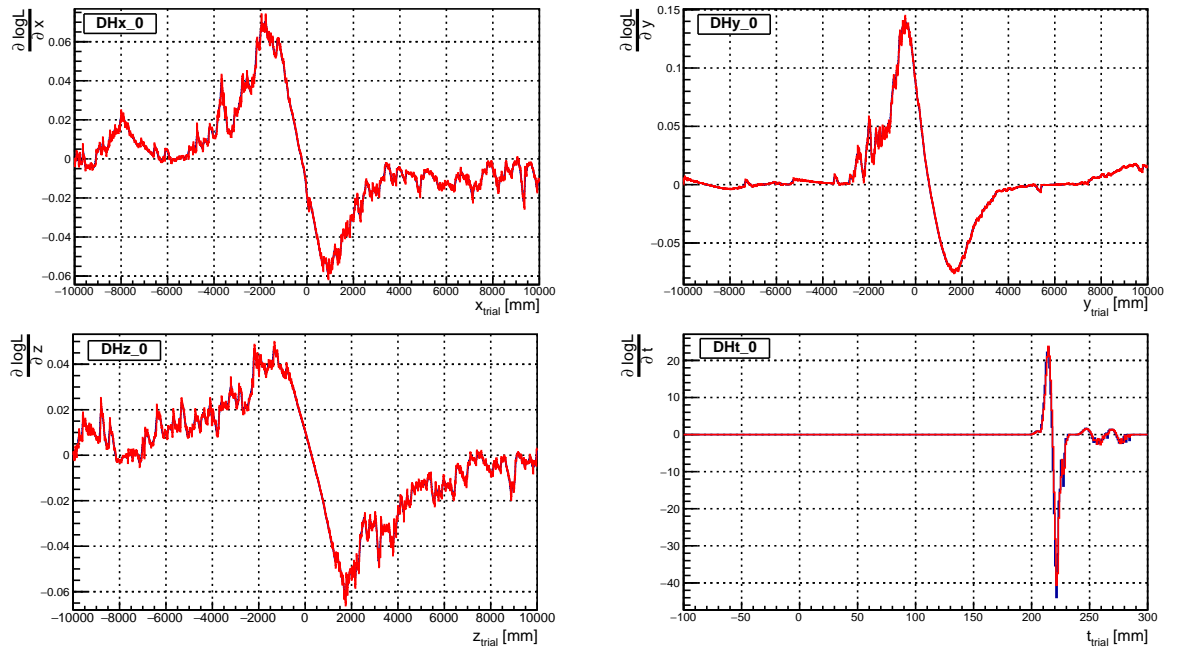
timing profile

scintillator timing

Figure 4.5: Derivatives of logLikelihood of an ^{16}N event projected on x, y, z, t axes. The analytical derivatives (blue) are overlaid with numerical derivatives (red). They are well-matched.

$$\sum_{i=1}^{n} A_i \cdot \frac{e^{-\frac{t}{\tau_i}} - e^{-\frac{t}{\tau_{rise}}}}{\tau_i - \tau_{rise}}$$

$$\{\sum_{i=1}^{n} A_i \cdot \frac{e^{-\frac{t}{\tau_i}} - e^{-\frac{t}{\tau_{rise}}}}{\tau_i - \tau_{rise}} * f_{PMT}(t - t')\} * Gaus(t, 0)$$

from bench top measurement, while the rise time, $t_{rise} = 0.8\ ns$ the timing parameters t_i, amplitude a_i are determined by the benchtop measurements

Table 4.2: scintillator α/β timing parameters**??**.

scintillator particles	timing [ns]				amplitudes			
	t_1	t_2	t_3	t_4	a_1	a_2	a_3	a_4
LAB + 2g/L PPO (default scintillator)								
e^-	4.88	15.4	66.0	400	0.665	0.218	0.083	0.0346
α	4.79	18.4	92.0	900	0.427	0.313	0.157	0.1027
LAB + 0.5g/L PPO (partial-fill phase)								
e^-	7.19	24.81	269.87	–	0.553	0.331	0.116	–
α	6.56	23.82	224.19	–	0.574	0.311	0.115	–
LAB + 2g/L PPO + 0.5% molar concentrations DDA								
e^-	5.0	12.1	33.3	499.0	0.68	0.21	0.07	0.04
α	3.8	11.3	65.3	758.0	0.48	0.32	0.14	0.06
LAB + 2g/L PPO + 0.5% molar concentrations Te+0.5% molar DDA								
e^-	3.7	10.0	52.0	500.0	0.72	0.23	0.02	0.03
α	3.69	15.5	79.3	489.0	0.63	0.23	0.07	0.07

pdfs

Radial bias is defined as the difference between the fitted and true position, projected along the radial component (unit vector) of the true position [14].

$$(\vec{X}_{fit} - \vec{X}_{true}) \cdot \hat{X}_{true}$$

The value of the mean radial bias is taken by fitting the histogram of the distributions of radial biases with a Gaussian profile and then get the mean of the fitted Gaussian profile.

Appendix: Levenberg-Marquardt method for fitter minimization (ref: press2007numerical)

for M unknown parameters: $a_0, a_1, ..., a_{M-1}$ (for example, the 4 parameters of an event vertex: (x, y, z, t))

the χ^2 function can be expanded and well approximated as

$$\chi^2(\mathbf{a}) \simeq \gamma - \mathbf{d} \cdot \mathbf{a} + \frac{1}{2}\mathbf{a} \cdot \mathbf{D} \cdot \mathbf{a},$$

$\mathbf{a}_{min} = \mathbf{a}_{cur} + \mathbf{D}^{-1} \cdot [-\nabla\chi^2(\mathbf{a}_{cur})]$

for a fudge factor λ,

$$\delta a_l = \frac{1}{\lambda\alpha_{ll}}\beta_l \ (\alpha_{ll} > 0),$$

$$\sum_{l=0}^{M-1} \alpha'_{kl}\delta a_l = \beta_k$$

Let $\alpha \equiv \frac{1}{2}\mathbf{D}$, which is the half Hessian, or called as curvature matrix.

$\beta_k = -\frac{1}{2}\frac{\partial\chi^2}{\partial a_k}, \ \alpha_{kl} = \frac{1}{2}\frac{\partial^2\chi^2}{\partial a_k \partial a_l}$

by optimizations, the values of tolerance, are set to .

4.6 PMT Selectors for the Fitter

- Straight Light Path TimeResidual Cut

  This selector is used for the direction reconstruction for the water phase.

- Mode cut

- Uniform PMT Selector

  Group PMTs by their positions. For azimuth angle Φ in $[-\pi, \pi]$, take n intervals; for zenith $\cos\theta$ in $[-1, 1]$, also take n intervals. This procedure divides the PMT sphere longitude and latitude.

  Then group PMTs in $n \times n$ panels.

  Pick up the PMTs uniformly and

  reduce the number of PMTs to a designated number to boost up the fit speed.
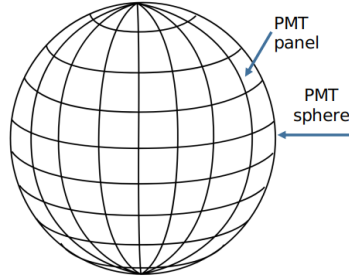
Figure 4.6: Group the PMTs by dividing the PMT sphere by latitudes and longitudes.

- Earliest Hit PMT Selector

  in prompt light time window For each panel, select PMTs with hitTime¿100 ns and then choose the earliest hit one. We can also set the other hit time window for the selected PMT in each panel. A similar selector which uses median hitTime for each panel has also been tested, but not as good as the earliest hit one.

  water phase fit speed for vertex reconstruction: 0.0017 s/call fit speed for direction reconstruction: 0.0004 s/call

4.7 ^{16}N Calibration

During the water phase, an Nitrogen-16 (^{16}N) calibration source was deployed for internal detector calibration scans in June and November, 2017 and external detector scans in March, 2018.

emit γ-rays. These γ-rays will Compton scatter off electrons and the electrons will emit Cherenkov light to be detected by the PMTs.

4.7.1 Water Phase Calibration

4.7.2 Partial-fill Phase Calibration

water level was at 5100 mm from the center of the AV (in AV coordination). LAB with a PPO concentration of 0.53 g/L

Effect of the water level.

The ^{16}N soure was deployed in the external water region during the partial-fill phase. run 251748 2019/09/19 and

Source position was at $(-1120.8, 1041.4, 6172.5)$ mm for a 30-minute duration and at $(-1120.8.1041.4, 6108.0)$ mm for a 7-hour duration (separated into 7 runs).

Chapter 5

SNO+ Water Phase Analysis

During the August to October 2019, the PPO is added into the LAB when the water level at 5100 mm (in PSUP coordinate). This is for the SNO+ partial-fill phase.

5.0.1 Sky-shine Classifier

A "sky shine" (SkyShine) classifier was developed by the collaboration to discriminate

The SkyShine classifier aims to discriminate "sky shine" events from other backgrounds by looking at the ratio of hit counts in a middle z range and a low z range. It can also look at neck and high-z OWL PMT hits. The classifier's behavior for partial fill is studied using simulation.

[39]

β_{14} isotropy classifier

$$\beta_l = \frac{2}{N(N-1)} \sum_{i=1}^{N-1} \sum_{j=i+1}^{N} P_l(\cos\theta_{ij})$$

where $P_l(\cos\theta_{ij})$ are Legendre polynomials

$\beta_{14} = \beta_1 + 4\beta_4$

thetaij isotropy classifier describes the angle subtended at an event vertex by PMT #i and PMT #j.

$$\cos\theta_{ij} = \frac{(\vec{X}_{PMT\#i} - \vec{X}_{event}) \cdot (\vec{X}_{PMT\#j} - \vec{X}_{event})}{|\vec{X}_{PMT\#i} - \vec{X}_{event}||\vec{X}_{PMT\#j} - \vec{X}_{event}|}$$

Chapter 6

Towards the SNO+ Future Phases

6.1 Partial-fill Phase Analysis

6.1.1 Bi-Po Analysis

Loop for events (loop 1, from first to last)

Event #i

FV cut & $Nhit_i \in (175, 1700)$

no

yes

Loop for the events (loop 2, from i+1 to last)

break loop 2

$\Delta t = t_j - t_i >$
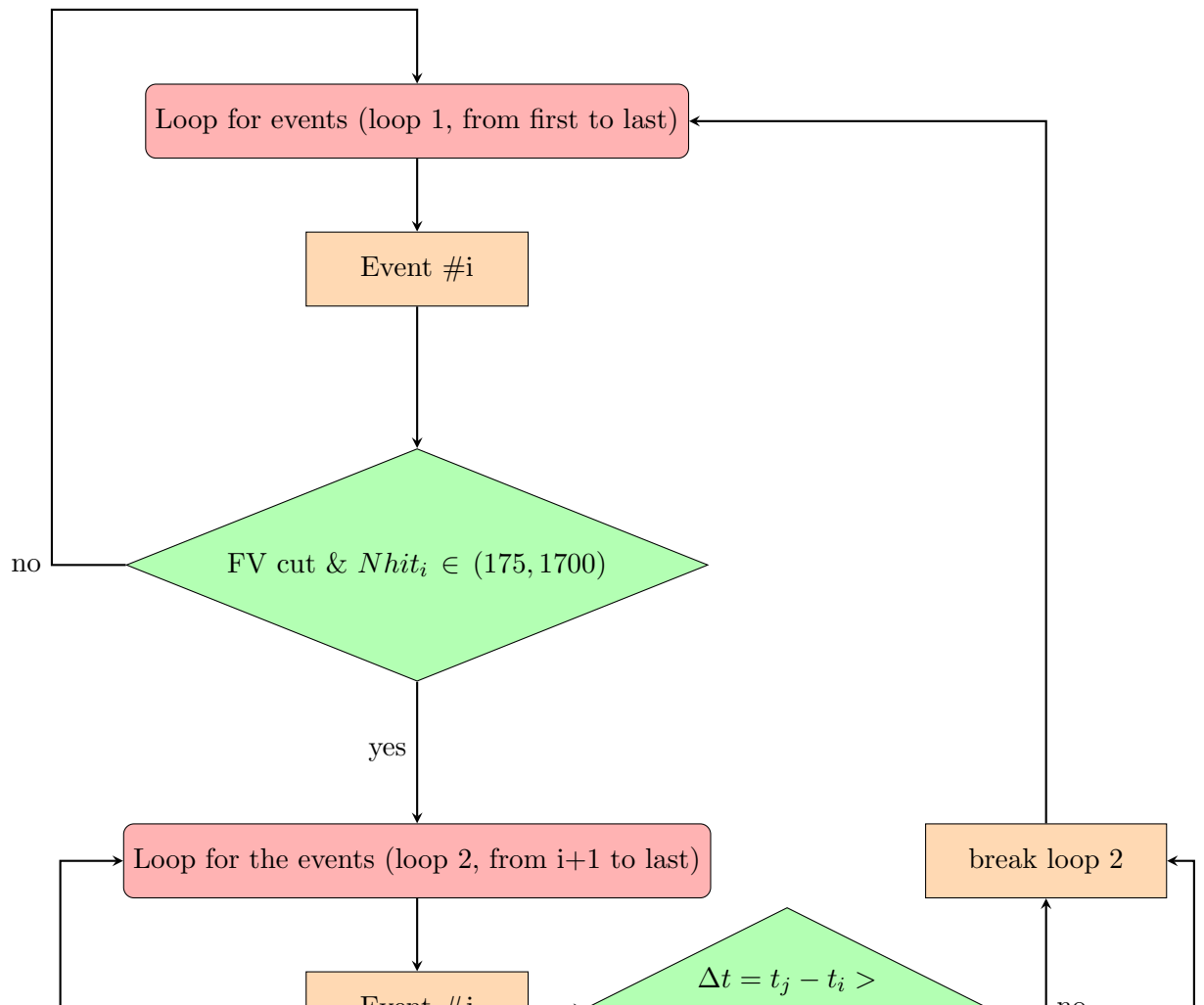
6.1.2 Extract Cherenkov Signals in Partial-Phase

^{16}N **Source Analysis**

$$\phi = \hat{\vec{v}}_e \cdot \hat{\vec{v}}_{assume}$$

$$\vec{n} = \hat{\vec{v}}_e \times \hat{\vec{v}}_{assume}$$

$$R = \begin{bmatrix} n_x^2(1-\cos\phi)+\cos\phi & n_x n_y(1-\cos\phi)-n_z\sin\phi & n_x n_z(1-\cos\phi)+n_y\sin\phi \\ n_x n_y(1-\cos\phi)+n_z\sin\phi & n_y^2(1-\cos\phi)+\cos\phi & n_y n_z(1-\cos\phi)-n_x\sin\phi \\ n_x n_z(1-\cos\phi)-n_y\sin\phi & n_y n_z(1-\cos\phi)+n_x\sin\phi & n_z^2(1-\cos\phi)+\cos\phi \end{bmatrix}$$

$$\vec{v'}_e = R\vec{v}_e$$

$$\vec{X'}_{evt} = R\vec{X}_{evt}$$

Move $\vec{X'}_{evt}$ to the origin,

$$\vec{X'}_{pmt} = R\vec{X}_{pmt} - \vec{X'}_{evt}$$

Breit-Wigner function

$$p(x) = \frac{c_0}{\pi} \frac{\frac{1}{2}\Gamma}{(x-m)^2 + (\frac{1}{2}\Gamma)^2} + c_1$$

AmBe **Source Analysis**

6.2 Relative Light Yield Measurements of the Te-loaded Liquid Scintillators

Chapter 7

Conclusions

SNO+ experiment

Appendix A

Details for the MultiPath Fitter

A.1   Create a Random Vertex

Four random seeds are generated from the uniform distribution function: $RandFlat$ in Class
Library for High Energy Physics (CLHEP) library.

One random seed is used for generating the time of the vertex: t is a random variable
following a uniform distribution in a range of $[100, 300]$ ns, say, $t \sim U(100, 300)$.

Three random seeds are used for generating the position of the trial vertex: $ran0 \sim$
$U(0, 1)$, $ran1 \sim U(-1, 1)$ and $ran2Pi \sim U(0, 2\pi)$.

Let $r = \sqrt[3]{ran0} * 10000$ mm, $\phi = ran2Pi$, $\cos\theta = ran1$ and $\sin\theta = \sqrt{1 - \cos^2\theta}$, then the
trial position can be built in Cartesian coordinate system: $\vec{x}_{trial} = (r\sin\theta\cos\phi, r\sin\theta\sin\phi, r\cos\theta)$.
This procedure ensures that a proper random position is generated inside a sphere with a
radius of 10 m.

A.2   Levenberg-Marquardt (MRQ) Method for Minimization[33]

Levenberg-Marquardt method is a common routine for non-linear fitting. Let $\mathbf{a} = [a_0, a_1, ..., a_{M-1}]^T$
be an M-dimensional vector with M unknown parameters to be fit, a χ^2 merit function
with the unknown parameter vector $\mathbf{a}$ can be built and by minimizing the function, the
best-fit $\mathbf{a}$ can be found.

The $\chi^2(\mathbf{a})$ can be approximately expanded into a quadratic form of Taylor-series:

$$\chi^2(\mathbf{a}) \simeq \gamma - \mathbf{d} \cdot \mathbf{a} + \frac{1}{2}\mathbf{a} \cdot \mathbf{D} \cdot \mathbf{a}, \tag{A.1}$$

where γ is a M-dimension constant vector around $\mathbf{a}$, $\mathbf{d}$ is a M-dimension vector and $\mathbf{D}$ is a $M \times M$ Hessian matrix.

To find a $\mathbf{a}_{min}$ so that a min $\chi^2(\mathbf{a}_{min})$ is reached, in computing science we usually use iteration steps:

$$\mathbf{a}_{min} = \mathbf{a}_{cur} + D^{-1}[-\nabla\chi^2(\mathbf{a}_{cur})], \tag{A.2}$$

where $\mathbf{a}_{cur}$ is the current trial value of $\mathbf{a}$ and we assume matrix $\mathbf{D}$ is invertible. The $\mathbf{a}_{cur}$ thus jumps onto $\mathbf{a}_{min}$.

According to the definition of a χ^2 merit function, it can be written out explicitly as: $\chi^2(\mathbf{a}) = \sum_{i=0}^{N-1}[\frac{y_i - y(x_i|\mathbf{a})}{\sigma_i}]^2$, with the same Taylor expansion, the quadratic form is written as:

$$\chi^2(\mathbf{a}) \approx \chi^2(\mathbf{a}_{cur}) + \sum_k \frac{\partial\chi^2(\mathbf{a}_{cur})}{\partial\alpha_k}\delta\alpha_k + \frac{1}{2}\sum_{kl} \frac{\partial^2\chi^2(\mathbf{a}_{cur})}{\partial\alpha_k\partial\alpha_l}\delta\alpha_k\delta\alpha_l, \tag{A.3}$$

where the first derivatives are:

$$\frac{\partial\chi^2}{\partial a_k} = -2\sum_{i=0}^{N-1}[\frac{y_i - y(x_i|\mathbf{a})}{\sigma_i}]\frac{\partial y(x_i|\mathbf{a})}{\partial a_k}, k = 0, 1, ..., M - 1, \tag{A.4}$$

and the second derivatives are:

$$\frac{\partial^2\chi^2}{\partial a_k\partial a_l} = 2\sum_{i=0}^{N-1}\{\frac{\partial y(x_i|\mathbf{a})}{\partial a_k}\frac{\partial y(x_i|\mathbf{a})}{\partial a_l} - [y_i - y(x_i|a)]\frac{\partial^2 y(x_i|\mathbf{a})}{\partial a_k\partial a_l}\}, k = 0, 1, ..., M - 1. \tag{A.5}$$

Let $\beta_k \equiv -\frac{1}{2}\frac{\partial\chi^2}{\partial a_k}, \alpha_{kl} \equiv \frac{1}{2}\frac{\partial^2\chi^2}{\partial a_k\partial a_l}$, then the factor of 2 is removed. The α_{kl} is defined as the curvature matrix and $\alpha = \frac{1}{2}\mathbf{D}$, which implies that it is the half of the Hessian matrix.

From A.2, we have: $D(\mathbf{a}_{min} - \mathbf{a}_{cur}) = [-\nabla\chi^2(\mathbf{a}_{cur})] \implies 2\alpha\delta\mathbf{a} = 2\beta$. The A.2 is now transformed into a systems of linear equations:

$$\sum_{l=0}^{M-1}\alpha_{kl}\delta a_l = \beta_k, \tag{A.6}$$

where δa_l is a varying amount added to the current value of parameter for the next iteration.

The main task now is to calculate α_{kl} and β_k and then solve for δa_l in A.6. Once δa_l is solved, we can vary the current trial or approximate values of $\mathbf{a}_{cur}$ and let it go close to or reach the $\mathbf{a}_{min}$.

If we consider the method of steepest descent: $\mathbf{a}_{next} = \mathbf{a}_{cur} - \text{const} \cdot \nabla \chi^2(\mathbf{a}_{cur})$, where const is a constant, then the δa_l is solved by

$$\delta a_l = \text{const} \cdot \beta_l, \tag{A.7}$$

where no Hessian matrix is needed.

In the Levenberg-Marquardt method, in order to solve for δa_l, the detailed calculation of $\mathbf{D}^{-1}$ in A.2 and the simplified calculation of steepest descent in A.7 are combined and a smooth transition between A.2 and A.7 is considered.

In A.7, the const describes the distance or magnitude of how far the parameter should go along the gradient β_l. From dimensional analysis, since $\beta_k \equiv -\frac{1}{2}\frac{\partial \chi^2}{\partial a_k}$ and χ^2 is a non-dimensional number, $[\beta_l] = [1/a_l]$. Then from A.7, $[\text{const}] = [a_l^2]$. The const has the same dimension to the term $1/\alpha_{ll} = 1/(\frac{1}{2}\frac{\partial^2 \chi^2}{\partial a_l \partial a_l})$, i.e., the diagonal elements in the curvature matrix. A bridge between A.2 and A.7 is thus built. The diagonal elements in the curvature matrix can control the magnitude of the const, tells how far the parameter should go along the gradient.

Then A.7 can be written as:

$$\delta a_l = \frac{1}{\lambda \alpha_{ll}}\beta_l \text{ or } \lambda \alpha_{ll} \delta a_l = \beta_l, \tag{A.8}$$

where α_{ll} is written in a form of $\alpha_{ll} = \sum_{i=0}^{N-1} \frac{1}{\sigma_i^2}[\frac{\partial y(x_i|\mathbf{a})}{\partial a_l}\frac{\partial y(x_i|\mathbf{a})}{\partial a_l}]$ to ensure that α_{ll} is always positive; a fudge factor λ can be set to $\lambda \gg 1$ to avoid the case when the value of const is taken too large.

Compare A.6 and A.8, if define a new curvature matrix, α' as the followings, these two equations can be combined:

$$\alpha' = \begin{cases} \alpha'_{jj} \equiv \alpha_{jj}(1 + \lambda) \, for diagonal elements \\ \alpha'_{jk} \equiv \alpha_{jk} \quad (j \neq k) \, for non-diagonal elements \end{cases} \tag{A.9}$$

References

[1] Multipath fitter processor. *SNO+ Internal Document, docDB-3849-v1*.

[2] Muons. `https://cosmic.lbl.gov/SKliewer/Cosmic_Rays/Muons.htm`, 2001. [Online; accessed 19-July-2019].

[3] Overview - rat 1.0 documentation. `https://rat.readthedocs.io/en/latest/overview.html#goals`, 2014. [Online; accessed 20-Dec-2019].

[4] S. Agostinelli, J. Allison, K. a. Amako, J. Apostolakis, H. Araujo, P. Arce, M. Asai, D. Axen, S. Banerjee, G. . Barrand, et al. Geant4a simulation toolkit. *Nuclear instruments and methods in physics research section A: Accelerators, Spectrometers, Detectors and Associated Equipment*, 506(3):250–303, 2003.

[5] M. Agostini, A. Bakalyarov, M. Balata, I. Barabanov, L. Baudis, C. Bauer, E. Bellotti, S. Belogurov, A. Bettini, L. Bezrukov, et al. Probing majorana neutrinos with double-β decay. *Science*, page eaav8613, 2019.

[6] C. Alduino, F. Alessandria, K. Alfonso, E. Andreotti, C. Arnaboldi, F. Avignone III, O. Azzolini, M. Balata, I. Bandac, T. Banks, et al. First results from cuore: A search for lepton number violation via $0\nu\beta\beta$ decay of te-130. *Physical review letters*, 120(13):132501, 2018.

[7] M. Anderson, S. Andringa, E. Arushanova, S. Asahi, M. Askins, D. Auty, A. Back, Z. Barnard, N. Barros, D. Bartlett, et al. Search for invisible modes of nucleon decay in water with the SNO+ detector. *Physical Review D*, 99(3):032008, 2019.

[8] M. Anderson, S. Andringa, S. Asahi, M. Askins, D. Auty, N. Barros, D. Bartlett, F. Barão, R. Bayes, E. Beier, et al. Measurement of the ^{8}B solar neutrino flux in SNO+ with very low backgrounds. *Physical Review D*, 99(1):012012, 2019.

[9] D. Auty and A. Hallin. Partial water fitter. *SNO+ Internal Document, docDB-2965-v2.*

[10] S. D. Biller, E. J. Leming, and J. L. Paton. Slow fluors for highly effective separation of cherenkov light in liquid scintillators. *arXiv preprint arXiv:2001.10825*, 2020.

[11] J. Birks and F. Firk. The theory and practice of scintillation counting. *Physics Today*, 18:60, 1965.

[12] M. G. Boulay. Direct evidence for weak flavour mixing with the sudbury neutrino observatory. 2004.

[13] R. Brun, F. Rademakers, P. Canal, et al. Rootan object oriented data analysis framework, 2007. *See Also http://root. cern. ch.*

[14] I. T. Coulter. *Modelling and reconstruction of events in SNO+ related to future searches for lepton and baryon number violation.* PhD thesis, University of Oxford, 2013.

[15] P. B. Denton, S. J. Parke, and X. Zhang. Eigenvalues: The rosetta stone for neutrino oscillations in matter. *arXiv preprint arXiv:1907.02534*, 2019.

[16] J. Dunger. *Topological and time based event classification for neutrinoless double beta decay in liquid scintillator.* PhD thesis, University of Oxford, 2018.

[17] I. Esteban, M. Gonzalez-Garcia, A. Hernandez-Cabezudo, M. Maltoni, and T. Schwetz. Global analysis of three-flavour neutrino oscillations: synergies and tensions in the determination of θ_{23}, δ_{CP}, and the mass ordering. *Journal of High Energy Physics*, 2019(1):106, 2019.

[18] M. Fukugita and T. Yanagida. *Physics of Neutrinos: and Application to Astrophysics.* Springer Science & Business Media, 2013.

[19] A. Giaz. Status and perspectives of the juno experiment. *arXiv preprint arXiv:1804.03575*, 2018.

[20] P. Gregory. *Bayesian Logical Data Analysis for the Physical Sciences: A Comparative Approach with Mathematica® Support*. Cambridge University Press, 2005.

[21] A. Hallin. Fitting partial fill data from december 2014. *SNO+ Internal Document, docDB-2888-v3*.

[22] G. Horton-Smith et al. Introduction to glg4sim, 2006.

[23] J. Hu and J. Tseng. Updates on the multipath water fitter 2018. *SNO+ Internal Document, docDB-4936-v2*.

[24] T. Kaptanoglu. Measurements of light yield and timing of 0.5 g/l lab+ppo. *SNO+ Internal Document, docDB-5997-v1*.

[25] T. Kaptanoglu. Characterization of the hamamatsu 8 r5912-mod photomultiplier tube. *Nuclear Instruments and Methods in Physics Research Section A: Accelerators, Spectrometers, Detectors and Associated Equipment*, 889:69–77, 2018.

[26] K. Kimura, A. Takamura, and H. Yokomakura. Exact formula of probability and cp violation for neutrino oscillations in matter. *Physics Letters B*, 537(1-2):86–94, 2002.

[27] G. F. Knoll. *Radiation detection and measurement*. John Wiley & Sons, 2010.

[28] L. D. Landau, J. Bell, M. Kearsley, L. Pitaevskii, E. Lifshitz, and J. Sykes. *Electrodynamics of continuous media*, volume 8. elsevier, 2013.

[29] P. Mekarski. Electron antineutrinos in the water phase of the sno+ experiment. 2018.

[30] B. A. Moffat. *The optical calibration of the Sudbury Neutrino Observatory*. PhD thesis, Ph. D. thesis, Queens University, 2001.

[31] J. Paton. Neutrinoless Double Beta Decay in the SNO+ Experiment. In *Prospects in Neutrino Physics (NuPhys2018) London, United Kingdom, December 19-21, 2018*, 2019.

[32] G. Piperno. Dark matter search with the cuore-0 experiment. 2015.

[33] W. H. Press, S. A. Teukolsky, W. T. Vetterling, and B. P. Flannery. *Numerical recipes 3rd edition: The art of scientific computing.* Cambridge university press, 2007.

[34] K. Singh. Wavelength shifter: Carbostyril 124. *SNO+ Internal Document, docDB-3351-v2.*

[35] K. Singh. Wavelength shifter in water phase of sno+. *SNO+ Internal Document, docDB-3869-v2.*

[36] A. Y. Smirnov. The msw effect and matter effects in neutrino oscillations. *Physica Scripta*, 2005(T121):57, 2005.

[37] A. Y. Smirnov. Solar neutrinos: Oscillations or no-oscillations? *arXiv preprint arXiv:1609.02386*, 2016.

[38] M. Tanabashi, K. Hagiwara, K. Hikasa, K. Nakamura, Y. Sumino, F. Takahashi, J. Tanaka, K. Agashe, G. Aielli, C. Amsler, et al. Review of particle physics. *Physical Review D*, 98(3):030001, 2018.

[39] J. Tseng. Skyshine classifier. *SNO+ Internal Document, docDB-5341-v1.*

[40] J.-S. Wang. Bipo analysis using partial fill data. *SNO+ Internal Document, docDB-5950-v3.*

[41] C. Weinheimer. Neutrino mass from triton decay. *Progress in Particle and Nuclear Physics*, 57(1):22–37, 2006.

[42] Z. Xing and S. Zhou. *Neutrinos in particle physics, astronomy and cosmology.* Springer Science & Business Media, 2011.

[43] Y. Xing-Chen, Y. Bo-Xiang, Z. Xiang, Z. Li, D. Ya-Yun, L. Meng-Chao, D. Xue-Feng, Z. Xuan, J. Quan-Lin, Z. Li, et al. Preliminary study of light yield dependence on lab liquid scintillator composition. *Chinese Physics C*, 39(9):096003, 2015.

[44] H. W. Zaglauer and K. H. Schwarzer. The mixing angles in matter for three generations of neutrinos and the msw mechanism. *Zeitschrift für Physik C Particles and Fields*, 40(2):273–282, 1988.

[45] K. Zuber. On the physics of massive neutrinos. *Physics Reports*, 305(6):295–364, 1998.